J Mater Sci: Mater Electron (2021) 32:752–763

Temperature stability of lead-free BST-BZN relaxor ferroelectric ceramics for energy storage capacitors

Zifeng He[1], Huiqin Li[1], Zhu Qing[1], Mengshi Zeng[1], Jun li[1], Lulu Zhou[1], Xiaoyan Zhong[1], and Jingsong Liu[1,*]

[1] *State Key Laboratory of Environment-Friendly Energy Materials, School of Materials Science and Engineering, Southwest University of Science and Technology, Mianyang 621010, People's Republic of China*

Received: 25 August 2020
Accepted: 6 November 2020
Published online: 16 November 2020

ABSTRACT

Low sintering temperature and good temperature stability are the crucial parameters for the actual application of the dielectric capacitors. In this work, lead-free relaxor ferroelectric ceramics with chemical formula $(1-x)(Ba_{0.4}Sr_{0.6})TiO_3$-$xBi(Zn_{2/3}Nb_{1/3})O_3$ [$(1-x)$BST-xBZN, (x = 0.00 to 0.225)] were developed through a solid-state synthesis route. The microstructures, dielectric performance, and temperature stability were studied in detail. The results show that 0.775BST-0.225BZN bulk ceramic with capacitance-temperature dependence satisfied with X8R specification can be obtained at a sintering temperature of 1140 °C. In addition, the energy storage performance of 0.775BST-0.225BZN bulk ceramic exhibits good temperature stability in a wide range of temperatures from 25 to 150 °C. High dispersion results in capacitance-temperature stability and energy storage stability. More importantly, the 0.775BST-0.225BZN ceramic also displays good charge–discharge performance dependence on temperatures (variations of the current density and power density are less than 3% over 25–150 °C). These results demonstrate that 0.775BST-0.225BZN lead-free ceramic is a potential material for dielectric capacitors that can be operated in a wide range of temperatures.

1 Introduction

In recent decades, pulsed power capacitors have been widely developed and applied in the energy storage industry. With the increasing demands of energy storage applications, the requirement for pulsed power capacitors with excellent dielectric properties has become an urgent task. Compared with chemical energy storage devices and superconducting magnetic energy storage systems, dielectric capacitors play a crucial role in pulsed power equipment on account of the excellent dielectric properties. Chemical energy devices, such as batteries, possess high energy density but low power density, while the dielectric capacitors exhibit the opposite features. The electrochemical capacitors have medium energy density and power density. Moreover, dielectric capacitors are more suitable for high-voltage, low-

Address correspondence to E-mail: feram@163.com

https://doi.org/10.1007/s10854-020-04854-x

cost, and large-scale applications. While the electrochemical capacitors can only suffer from the low operating voltage (< 3 V), large leakage current, and high cost [1–5] Moreover, they could be applied in a wide range of temperatures due to their good stabilization of the capacitance-temperature [4].

Generally, lead-based ceramics present excellent dielectric properties [6, 7], such as large polarization and high breakdown strength (BDS), but their possible toxicity limits their applications in the future. Thus, the lead-free ceramics gradually attracted the attention of researchers owing to the environmental friendliness, high BDS, and a relatively low dielectric loss. Among them, perovskite $Ba_xSr_{1-x}TiO_3$ (BST) comes from $SrTiO_3$ (ST) and $BaTiO_3$ (BT) which shows excellent properties, for example, low hysteresis loss and a relatively high energy storage density. To satisfy the growing demands of the dielectric capacitors, especially the ceramic capacitors, studies have aimed at improving the performance of the energy storage [6, 8–15]. For instance, $Ba_{0.4}Sr_{0.6}TiO_3$ ceramics were reported in many publications showing excellent dielectric properties, such as good dielectric stability and moderate permittivity, for the application of energy storage equipment [1, 12, 15–19]. The $(Sr_{0.4}Ba_{0.6})_{0.925}Bi_{0.05}TiO_3$ ceramics have been reported with high dielectric constant and high tunability that were sintered for 4 h at 1260 °C [1]. Furthermore, Diao et al. have reported that $Ba_{0.4}Sr_{0.6}TiO_3$-0.45wt% SiO_2 ceramics sintered for 2 h at 1330 °C showed excellent properties of the energy storage density (W_{st}) and the release efficiency (η) at 134 kV/cm [19]. Additionally, it was reported that the $(Ba_{0.4}Sr_{0.6})TiO_3$ ceramics with grain size on the order of 0.5 μm possess a BDS of 243 kV/cm, much higher than that of ceramics with the grain size of 5.6 μm, which is on the order 114 kV/cm [13]. W.B. Li et al. have reported that $0.9BaTiO_3$-$0.1Bi(Mg_{2/3}Nb_{1/3})O_3$ ceramics modified by 0.3wt% $MnCO_3$ and the $0.85BaTiO_3$-$0.15Bi(Zn_{2/3}Nb_{1/3})O_3$ ceramic exhibited good energy storage properties, respectively [20, 21]. Other approaches were also applied to improve the dielectric performances, such as thermal annealing [17], spark plasma sintering [10], and grain size controlling [15].

The previous reports indicated that excellent energy storage density and high BDS of BST-based ceramics have been achieved. However, BST-based ceramics with excellent properties of W_{st} and η still require the support of high sintering temperatures. High sintering temperature means large energy consumption. Thus, Reducing the sintering temperature of ceramics not only can save energy, but also lower the cost. Besides, the temperature stability cannot be ignored due to the harsh working environment of the dielectric capacitor. However, few works are focused on the temperature stability and lowering the sintering temperature for BST-based ceramics.

BT-$Bi(Me)O_3$, BST-$Bi(Me)O_3$ (Me = $(Zn_{1/2}Ti_{1/2})^{3+}$, $(Mg_{1/2}Ti_{1/2})^{3+}$, etc.) ceramics have been reported widely due to Bi^{3+} can improve the dielectric performances, and Me ions are adjustable [14, 21, 22]. In this work, $Bi(Zn_{2/3}Nb_{1/3})O_3$ has been selected to improve the characteristics of the $Ba_{0.4}Sr_{0.6}TiO_3$ ceramics. On the one hand, the introduction of Bi^{3+} not only can effectively reduce the sintering temperature but also improve the temperature stability of the BST ceramics. On the other hand, an appropriate amount of incorporation with ZnO and Nb_2O_5 can reduce the sintering temperature and adjust the microstructure of the BST ceramics.

In this work, lead-free $(1-x)$BST-xBZN, x = 0.00 to 0.225, bulk ceramics were synthesized via the solid-state route. Moreover, the microstructures, dielectric performances, and temperature stability of the prepared ceramics were discussed systematically. The capacitance-temperature dependence satisfied with X8R specification (from − 55 to 150 °C, the capacitance varies within ± 15%, which is defined by the Electronics Industry Alliance.) and sintering temperature of 1140 °C was obtained in 0.775BST-0.225BZN lead-free ceramic.

2 Experimental procedure

A series of lead-free $(1-x)$BST-xBZN bulk ceramic samples were synthesized through the traditional solid-state synthesis route. High-purity powers(> 99.9%) were used as the raw materials including $BaCO_3$, $SrCO_3$, TiO_2, Bi_2O_3, ZnO, and Nb_2O_5. According to the stoichiometric formula of $(1-x)(Ba_{0.4}Sr_{0.6})TiO_3$-$xBi(Zn_{2/3}Nb_{1/3})O_3$ [$(1-x)$BST-xBZN, (x = 0.00 to 0.225)], the powders were mixed and milled for 6 h in a polyurethane tank with zirconia balls and ultrapure water as the solvent. After the slurry drying, the obtained dried powders were calcined for 3 h at 1000 °C. Whereafter, with the same conditions as described above, the powders were ball-milled again for 24 h. Subsequently, a 5wt%

solution of PVA was mixed with the obtained powders, which was subsequently pressed into cylinders under the pressure of 250 MPa. Finally, the pellets were put into a closed alumina crucible with powders having the same composition as the samples to diminish the evaporation of volatile elements, and sintered for 2 h at 1140–1250 °C after burning off the PVA adhesive.

Structures were researched via the X-ray diffraction (DMAX, Netherlands). The local structure distortions were recorded by Raman scattering spectrometer (Renishaw, London, UK) at 100 cm^{-1} to 1000 cm^{-1}. Using SEM (Carl Zeiss NTS GmbH, Germany) to observe the ceramics for their surface morphologies. The temperature dependence of dielectric properties was recorded by an impedance analyzer (WAYNE KERR 6500B, UK) equipped with a temperature control system (VDMS2000, China). The *P-E* loops of all ceramics, which can be recorded by a ferroelectric test system (TF analyzer 2000, USA). The discharge current waveforms were obtained by an RLC discharge circuit test system with an oscilloscope (Tongguo (TG) technology, Pulsed Charge–discharge System, CFD-003).

3 Results and discussion

3.1 Phases and microstructure

Figure 1 displays the XRD patterns for the prepared ceramics. Figure 1a exhibits that the main diffraction peaks are assigned to the perovskite pseudocubic phase, and the second phase (JCPDS#28-1243, $SrNb_2O_6$) can be observed when the content of BZN level up to 0.15. A solid solution was obtained as the content at $x < 0.15$, and then a new phase $SrNb_2O_6$ appears while $x \geq 0.15$. Chen et al. revealed that the A-site ions were occupied by Bi^{3+}, on account of the similar ion radius between Bi^{3+} and Ba^{2+}, and then a finite solid solution in $(Sr_{0.4}Ba_{0.6})_{1-1.5x}Bi_xTiO_3$ can be formed [1]. Obviously, the appearance of the new phase $SrNb_2O_6$ is attributed to exceeding of the solid solubility limit.

Figure 1b shows that the (200) diffraction peaks display a gradually shifting to the low angle as the BZN content increases, which manifests the large interplanar spacing. The coordination numbers of the cations (Ba^{2+}, Sr^{2+}, Bi^{3+}) and the ions (Ti^{4+}, Zn^{2+}, Nb^{5+}) are 12 and 6, respectively. Most likely, the Zn^{2+} and Nb^{5+} ions are probably entering into the B-sites to substitute for Ti^{4+} ions (0.0605 nm). In addition, Ba^{2+} ions (0.161 nm) and Sr^{2+}(0.112 nm) of 12-fold coordination at A-sites are substituted by Bi^{3+} ions (0.144 nm). Obviously, the substitution can occur only between those ions with a similar radius.The effective radius of $(Zn_{2/3}Nb_{1/3})^{3+}$ is counted as $r = (2/3)r(Zn^{2+}) + (1/3)r(Nb^{5+}) = 0.0707$ nm (the ionic radius of Zn^{2+}, Nb^{5+}, and Ti^{4+} is 0.074, 0.064, 0.0605 nm, respectively) [2, 3]. To further study the crystal structure transformation caused by $(Zn_{2/3}Nb_{1/3})^{3+}$ substitution, Raman spectra at 100–1000 cm^{-1} were carried out.

Figure 2 plots the Raman spectra measured at the range from 100 to 1000 cm^{-1}. The main peaks of Raman spectra are located at above 600 cm^{-1}, 400–600 cm^{-1}, 200–400 cm^{-1}, and below 200 cm^{-1}. For perovskite structure, the peaks under 200 cm^{-1} are induced by the vibrations of the ions at A-sites (Ba^{2+}, Sr^{2+}, Bi^{3+}) [12, 23]. It is found the peak at $\sim$ 148 cm^{-1} that can be vested in the vibration of Sr–O and Ba–O bonds decreases in intensity with the increases of x value [24]. The peak at about 190 cm^{-1}, which means that some Sr^{2+} have been substituted by Bi^{3+} and Ba^{2+} [25]. For Bi^{3+}-doped perovskite ceramics, the disorder of the A-sites could be increasing, and then the relaxor behavior appears [25–27]. According to the above discussion, it can be believed that the peaks of $\sim$ 190 cm^{-1} reveal a part of the relaxor source for the inequitable substitution at the A-site. The vibration of B-O is related to the A_1 (TO_2) mode at $\sim$ 270 cm^{-1}. The A_1 (TO_3) mode at $\sim$ 516 cm^{-1} within the scope of 400–600 cm^{-1} is caused by the vibrations of the TiO_6 octahedron [24]. As the content of x increases, it is found that the peaks at $\sim$ 516 cm^{-1} progressively become widened. This phenomenon is raised by the short-range distorted TiO_6 octahedron induced by the occupation of Zn^{2+} and Nb^{5+} ions for Ti^{4+}. Moreover, the peaks at 780 cm^{-1} are on account of the vibration of A_1 (LO_3) and E (LO) overlapped modes [7]. The result of the Raman spectra is well consistent with the above analysis of XRD.

Figure 3 shows the surface morphologies and the energy-dispersive X-ray spectroscopy (EDAX) for the samples. It can be seen that a few pores were observed on the surface of pristine BST ceramic in Fig. 3a. As shown in Fig. 3b, a dense microstructure and the second phase can be observed in the 0.775BST-0.225BZN ceramic. It can be seen that the

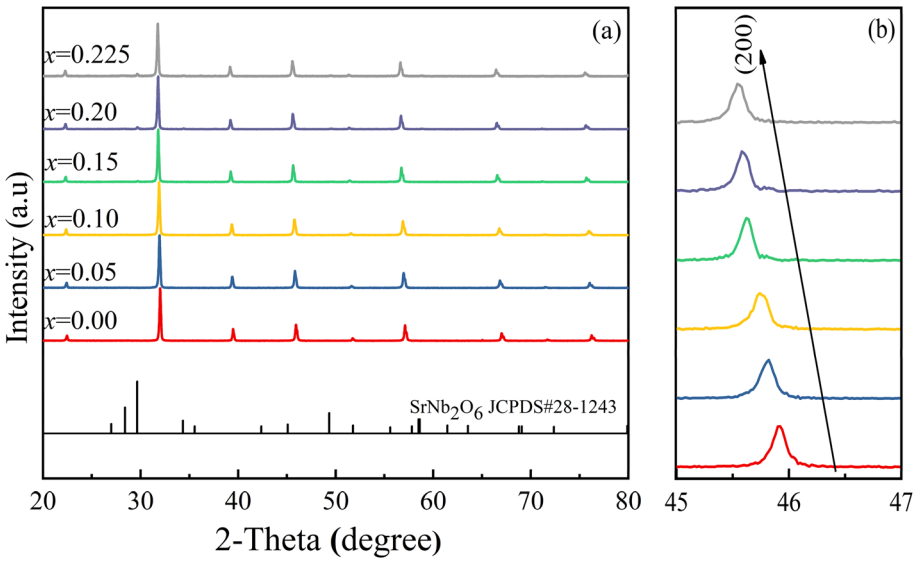

Fig. 1 **a** XRD patterns of the $(1-x)$BST-xBZN ceramics with the increase of BZN content recorded at room temperature; **b** their detailed comparison in 2 Theta range from 45° to 47°

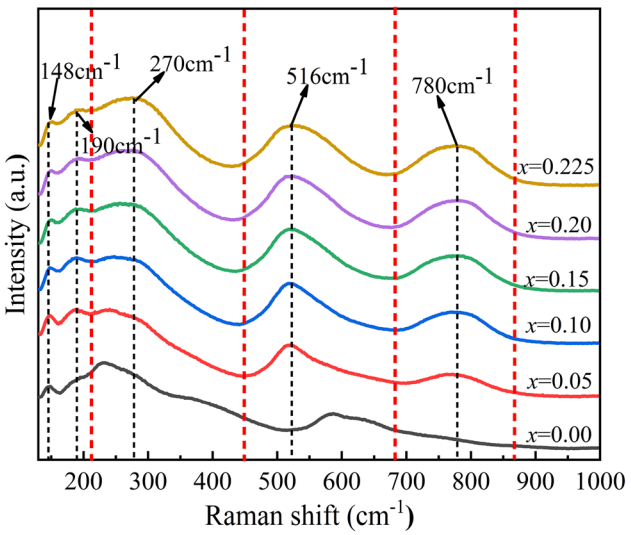

Fig. 2 The Raman spectra of the $(1-x)$BST-xBZN ceramics were recorded at room temperature from 100–1000 cm^{-1}

grain size of $(1-x)$BST-xBZN ceramics increases with increasing the value of x. The obvious change in the microstructure might be related to the fact that A-site and B-site elements such as Bi^{3+} and Zn^{2+} in $(1-x)$BST-xBZN ceramics volatilize inevitably due to their low melting points [7], leading to the presence of oxygen vacancies, which is beneficial to mass transportation during sintering [22, 28]. From Fig. 3c and d, the EDAX analyses of the samples show that the 0.775BST-0.225BZN ceramic exhibits the cooccurrence of the BST phase with the second $SrNb_2O_6$ phase, which accord with the consequence of the XRD patterns.

From the above analyses, it can be concluded that the introduction of BZN modified the microstructure. The electrical property may be affected by the value of BZN. The change of the microstructure will further influence the dielectric performance of the $(1-x)$BST-xBZN samples. Next, the dielectric performances were studied in detail.

3.2 Dielectric performances analysis

The dielectric performance dependence on temperature (− 140 °C to 150 °C) for all samples was recorded at the test ranges of 1 kHz–1 MHz, and the results are presented in Fig. 4. It can be observed that the permittivity has a deeply decreased with the BZN content increased, which can be attributed to that the BZN possesses a lower permittivity than that of the pristine $Ba_{0.4}Sr_{0.6}TiO_3$ ceramics [22]. Obviously, with the increase of BZN content, T_m moves to a low direction at first and then shifts toward high temperatures. The dielectric characterization of all composition revealed a gradual change from normal ferroelectric behavior to high diffusive relaxor-like characteristics, which may be explained by the weak orbital hybridization of Mg–O destroyed the long-range Coulomb potential in the crystal. Furthermore, as reported, the Curie temperature of $SrNb_2O_6$ is around 300 °C, which may contribute to the increase of the T_m of the $(1-x)$BST-xBZN samples [29]. The dielectric property of all ceramics means a gradual high diffusive relaxor-like behavior as the content of BZN increases. This phenomenon may be explained

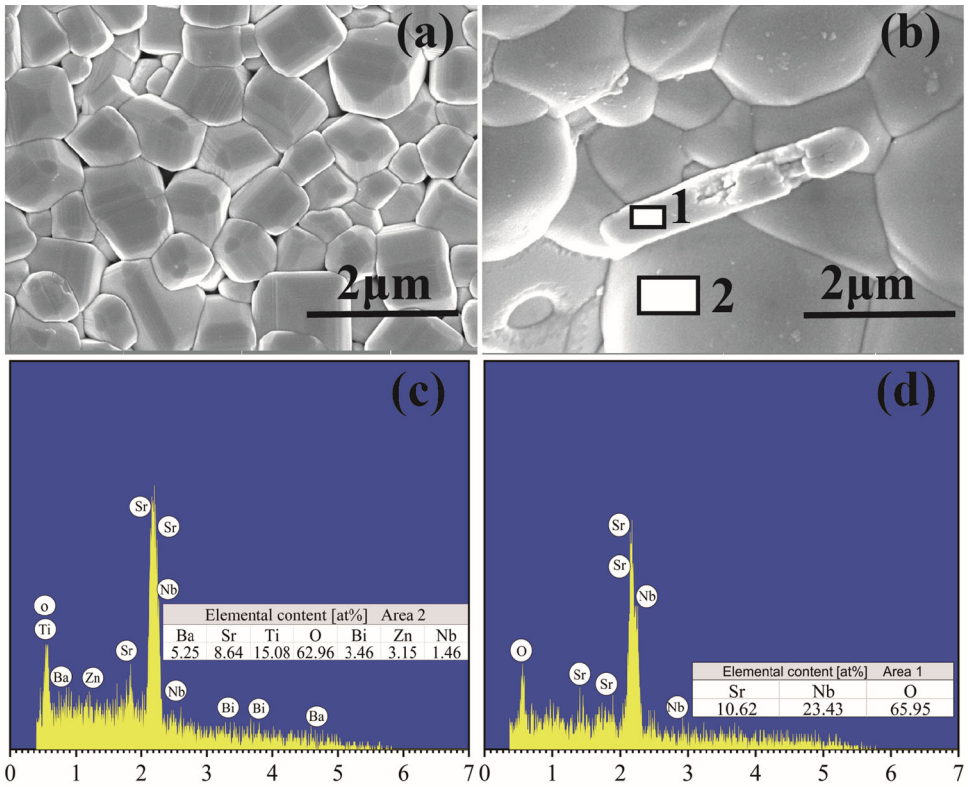

Fig. 3 SEM of the $(1 - x)$BST-xBZN ceramics: **a**, $x = 0.00$; **b**, $x = 0.225$. EDAX of the $(1 - x)$BST-xBZN ceramics: **c** and **d** are selected in different area

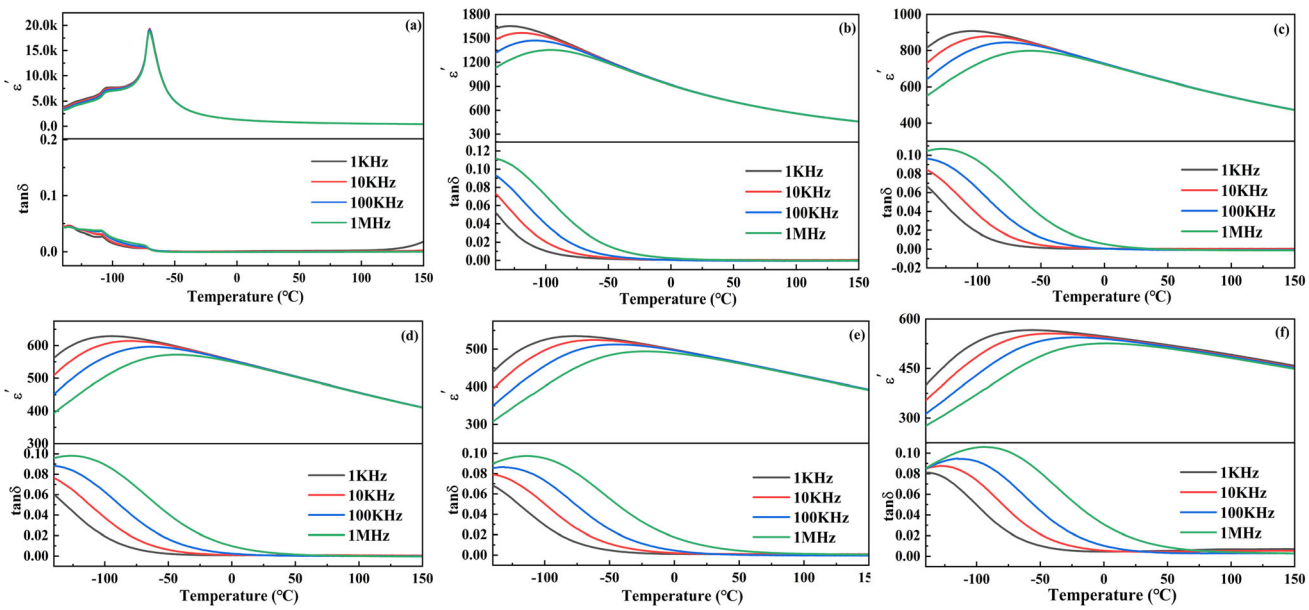

Fig. 4 Temperature dependence of dielectric constant and dielectric loss for the $(1 - x)$BST-xBZN ceramics measured from 1 kHz to 1 MHz: **a** $x = 0.00$, **b** $x = 0.05$, **c** $x = 0.10$, **d** $x = 0.15$, **e** $x = 0.20$, **f** $x = 0.225$

via the disorder of A-sites are substituted by Bi^{3+} and Ba^{2+} [30]. On the other hand, the relaxor behavior can also be explained via the long-range dipole action that was destroyed by the Ti^{4+}, Zn^{2+}, Nb^{5+} with different charges at B-site [31]. It should be noted that the dielectric constant and dielectric loss exhibit strong frequency dispersion behavior and the dielectric constant plateau of the ceramics. Therefore, it is rationalized that $(1 - x)$BST-xBZN ceramics are a typical relaxor ferroelectrics [32]. As the increase of

BZN content, the curve becomes more and more gentle in the tested temperature ranges. This phenomenon indicates the optimization of temperature stability. Next, for all of the samples, the capacitance-temperature variations and the relaxation characteristics are further investigated.

The graphs of capacitance variation with temperature are given in Fig. 5a. The samples show good temperature stability with the increasing content of BZN. When the BZN content is 0.225, the capacitance-temperature variation satisfies the X8R specification (from − 55 to 150 °C, the capacitance varies within ± 15%, which is defined by the Electronics Industry Alliance.). The generation of the $SrNb_2O_6$ (T_m ~ 300 °C) can influence the optimization of dielectric temperature characteristics, which flats the T_m peaks of the samples.

A Curie–Weiss formula [7, 24, 27] was introduced to further study the diffuse character of the (1 − x)BST-xBZN ceramics, as follows:

$$\frac{1}{\varepsilon'_\gamma} - \frac{1}{\varepsilon'_m} = \frac{(T - T_m)^\gamma}{C} \quad (1)$$

C represents the Curie constant. Where ε'_γ represents the permittivity at the temperature of T and ε'_m is the peak value of permittivity, respectively. T_m represents the corresponding temperature at the maximum value of the permittivity [24, 33]. The γ represents the diffusion index. $\gamma = 1$ and $\gamma = 2$ represents a typical ferroelectric and a complete disorder, respectively. When $1 < \gamma < 2$, the typical relaxation behavior accompanied by the dispersion phase transition is found. The value of γ is obtained by fitting the test data at 1 kHz through Eq. (1). It can be observed that the value of γ for all ceramics increased from 1.22 to 1.56, 1.59, 1.68, 1.70, 1.76 with the BZN content increased from 0.00 to 0.225. This phenomenon indicates the typical transition to relaxor ferroelectric from ferroelectric, which is beneficial to improving the energy storage efficiency and reducing the remanent polarization of the ceramics.

The P-E hysteresis loops of the specimens were recorded under an electric field of 170 kV/cm at a tested frequency of 10 Hz as shown in Fig. 6a. The value of the remanent polarization (P_r), energy storage density (W_{st}), maximum polarization (P_{max}), releasable efficiency (η) is listed in Table 1. As shown in Fig. 6a, the W_{st} of the 0.95BST-0.05BZN ceramic is 0.953 J/cm^3, which is almost 3 times more than that of pristine $Ba_{0.4}Sr_{0.6}TiO_3$ ceramic [15–17]. As the BZN content increases, the P_{max} declines from 10.92 to 7.03 μC/cm^2 and a deep fluctuation from 0.91 to 0.17 μC/cm^2 of the P_r, as shown in Table 1. The P_{max} sharply decreased as the x content increases, it can be ascribed to the long-range dipole action that was destroyed by the Ti^{4+} and Nb^{5+} with different charges at B-site [31], and then the relaxation behavior was enhanced as the BZN value increases. W_{st} was calculated via polarization–electric filed loops in Fig. 6a, and the W_{st} has a deep reduction with the x value increases. Meanwhile, the η sharply increases to 92.90% from 77.58% with the increasing BZN value. As shown in Fig. 5, the value of γ increases from 1.56 to 1.76 as the BZN content increases from 0.05 to 0.225 at the temperature range of − 55 °C to 150 °C, indicating the typical transition to relaxor

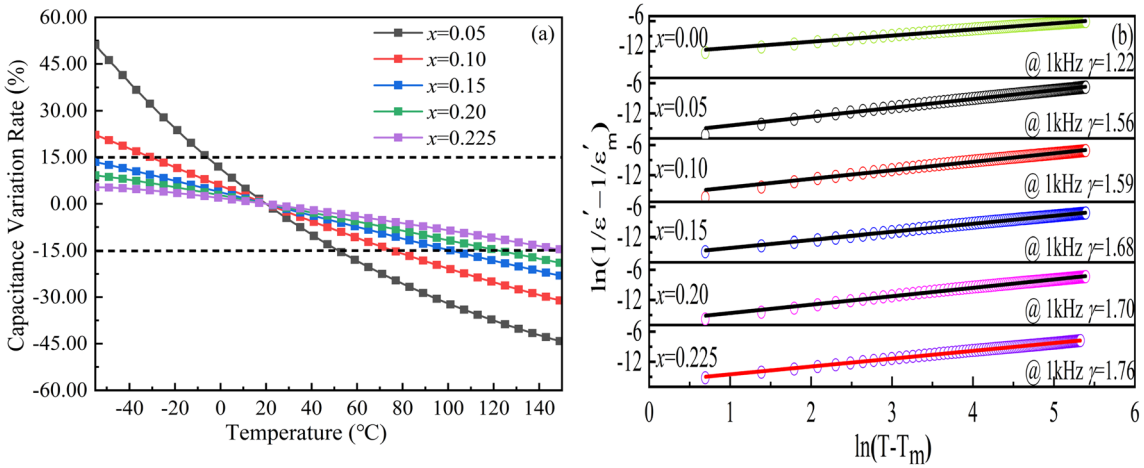

Fig. 5 Dielectric properties of the (1 − x)BST-xBZN ceramics. **a** Temperature dependence of capacitance variation rate of the (1 − x)BST-xBZN ceramics. **b** The diffuseness parameter γ for the (1 − x)BST-xBZN ceramics measured at 1 kHz

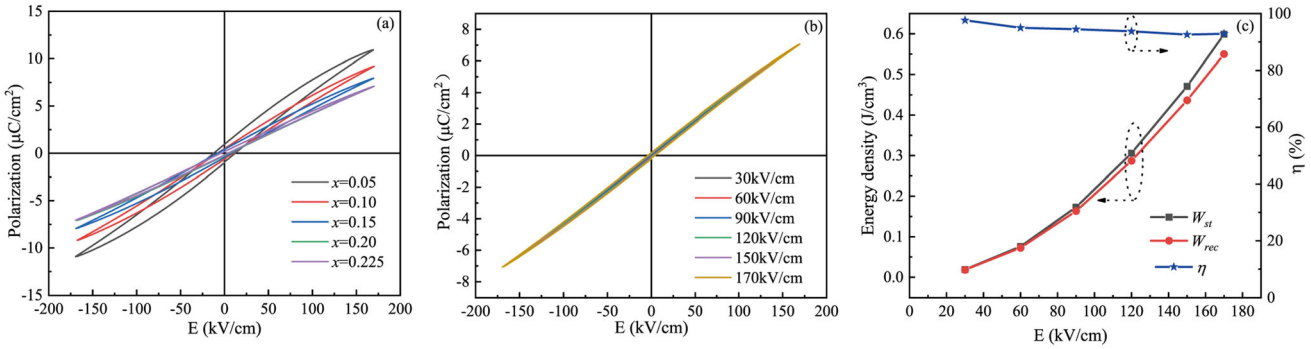

Fig. 6 **a** The *P-E* hysteresis loop of the (1-*x*)BST-*x*BZN ceramics at 170 kV/cm; **b** The hysteresis loop and **c** the energy storage properties of 0.775BST-0.225BZN ceramic at room temperature and 10 Hz under different electric fields

Table 1 The energy storage parameters of the $(1-x)$BST-xBZN ceramics at 170 kV/cm

$(1-x)$BST-xBZN	P_{max} (μC/cm^2)	P_r (μC/cm^2)	W_{st} (J/cm^3)	η (%)
x = 0.05	10.92	0.91	0.953	77.58
x = 0.10	9.19	0.48	0.797	85.30
x = 0.15	7.94	0.41	0.685	87.24
x = 0.20	7.08	0.21	0.631	91.80
x = 0.225	7.03	0.17	0.620	92.90

ferroelectric from ferroelectric. So, as the x value increase, the η become larger. This is attributed to the normal ferroelectric has a large hysteresis loss compared with the relaxor ferroelectric, as shown in Fig. 6a.

Figure 6b presents the *P-E* hysteresis loops of the 0.775BST-0.225BZN sample. A slim *P-E* hysteresis loop is obtained with the increase of the electric field, indicating the higher efficiency. Table 2 exhibits the energy storage characteristics of the 0.775BST-0.225BZN sample tested in different electric fields. From Fig. 6c and Table 2, it can be found that the W_{st} increases with the increase of the electric field. Moreover, the η remains as high as 92% with the electric field increases, indicating a relatively high release efficiency of the 0.775BST-0.225BZN ceramic. The W_{st} is nearly proportional to the square of E. Predictably, the W_{st} will increase to ~ 1 J/cm^3 when the applied electric field is larger than 200 kV/cm due to the large P_{max} and low P_r.

Table 2 The energy storage parameters of the 0.775BST-0.225BZN ceramic in different electric fields

E (kV/cm)	P_{max} (μC/cm^2)	P_r (μC/cm^2)	W_{st} (J/cm^3)	η (%)
30	1.25	0.01	0.019	97.65
60	2.52	0.03	0.076	95.00
90	3.80	0.07	0.173	94.48
120	5.07	0.12	0.306	93.74
150	6.28	0.15	0.471	92.59
170	7.03	0.17	0.620	92.90

The temperature stability of the energy density cannot be ignored due to the harsh working environment of the dielectric capacitor. To further investigate the temperature stability of the energy storage, the hysteresis loops of 0.775BST-0.225BZN ceramic were obtained in the diverse temperatures. Figure 7a, b indicates the energy storage performances of 0.775BST-0.225BZN ceramic in the temperatures range of 25 °C to 150 °C at 10 Hz and 170 kV/cm. A series of slim *P-E* hysteresis loops were obtained in the tested range of temperatures. Table 3 lists the temperature parameters of the energy storage characteristics. As the temperature increases, it can be observed that the value of P_{max} decreases slightly from 7.03 to 5.96 μC/cm^2, which indicates the energy storage density has a slight fluctuation in the high-temperature region. The appearance of nonpolar phases may result in a decrease in P_r at high temperatures [34–36]. The W_{st} of the 0.775BST-0.225BZN ceramic in Fig. 7b is smaller than the W_{st} in Fig. 6a with the temperature increases, this is because the P_{max} has a slightly decreased with the same electric fields. From Fig. 7b, it can be found that the W_{st} of the

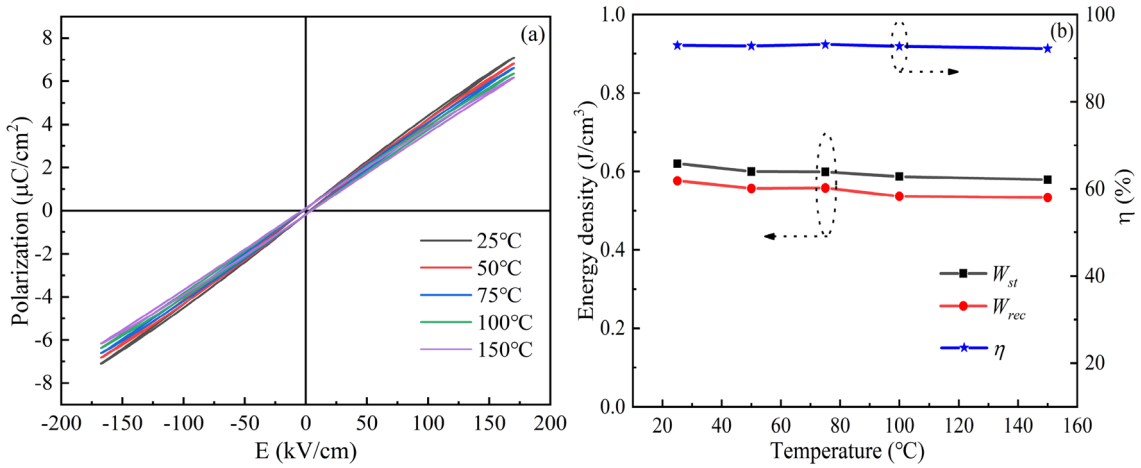

Fig. 7 **a** The hysteresis loop of 0.775BST-0.225BZN ceramic with different temperatures under 170 kV/cm; **b** The energy storage and release efficiency of the 0.775BST-0.225BZN ceramic

Table 3 The energy storage parameters of the 0.775BST-0.225BZN ceramic at 170 kV/cm with different temperatures

Temperature (°C)	P_{max} (μC/cm^2)	P_r (μC/cm^2)	W_{st} (J/cm^3)	η (%)
25	7.03	0.17	0.620	92.90
50	6.91	0.125	0.600	92.76
75	6.52	0.113	0.592	93.10
100	6.31	0.118	0.587	92.69
150	5.96	0.124	0.578	92.16

0.775BST-0.225BZN ceramic exhibits good temperature stabilize (does not exceed 7%) and the η remains as high as 92% in a very wide range of temperatures from 25 to 150 °C, which suggests good energy storage stabilization. As shown in Fig. 5, the 0.775BST-0.225BZN ceramic meets the X8R specification, indicating the capacitance has good stability in the tested range of temperatures. Besides, the permittivity is proportional to the capacitance. The dielectric constant reflects the polarization behavior of the dielectric indicating the polarization has a good stabilization on temperature. The value of γ is 1.76 as the BZN content is 0.225 and a high diffuse phase transition appears. A high diffuse phase transition means that the reversal of polarization keeps a good stabilization on temperature. So, it is reasonably obtained good temperature stability on energy storage of the 0.775BST-0.225BZN ceramic at the tested range of temperatures. The energy storage performances of the 0.775BST-0.225BZN ceramic compared with other BST-based ceramics are listed in Table 4, suggesting excellent temperature stability of the 0.775BST-0.225BZN ceramic.

The charge–discharge properties of the pulse capacitors can not be ignored in the actual application environment. The discharge current waveforms of the 0.775BST-0.225BZN ceramic were obtained at the diverse electric fields in the underdamped stage as shown in Fig. 8a, which are typical sinusoidal. Figure 8b presents the peak current value, power density ($P_D = EI_{max}/2S$) and current density ($C_D = I_{max}/S$) of the 0.775BST-0.225BZN ceramic under the diverse electric fields. It can be found that the peak current value increases from 13 to 70 A and the maximum current density up to 357 A/cm^2 with the electric field increases to 170 kV/cm. Correspondingly, the 0.775BST-0.225BZN ceramic has a large power density of 30 MW/cm^3.

From an application point of view, the good temperature stability of the charge–discharge properties is another important character for the pulse capacitors in the harsh working environment. As shown in Fig. 8c and d, the peak current value, the current density, and the power density of the 0.775BST-0.225BZN ceramic has a slight fluctuation in a wide temperature range of 25 °C to 150 °C. This result can be attributed to the good temperature stability of

Table 4 Comparison of energy storage properties of other ceramics with the 0.775BST-0.225BZN ceramic in this work

Composition	E (kV/cm)	W_{st} (J/cm^3)	η (%)	X8R or better	Refs
90wt%$BaTi_{0.85}Sn_{0.15}O_3$-10 wt%MgO	190	0.51	92.11	No	[37]
99.5wt%$Ba_{0.4}Sr_{0.6}TiO_3$-0.5 wt%SiO_2	134	0.86	79	No	[19]
0.8$Sr_{0.875}Pb_{0.125}TiO_3-0.2Bi(Mg_{0.5}Zr_{0.5})O_3$	150	0.762	96.34	No	[7]
95 wt%$Ba_{0.4}Sr_{0.6}TiO_3$-5 wt%BBZ	145	0.62	–	No	[11]
BNT-BT-0.32SBT	60	0.5	90	No	[35]
0.925SPBT-0.075BIT	80	0.252	82.02	No	[6]
0.775BST-0.225BZN	170	0.620	92.9	Yes	This work

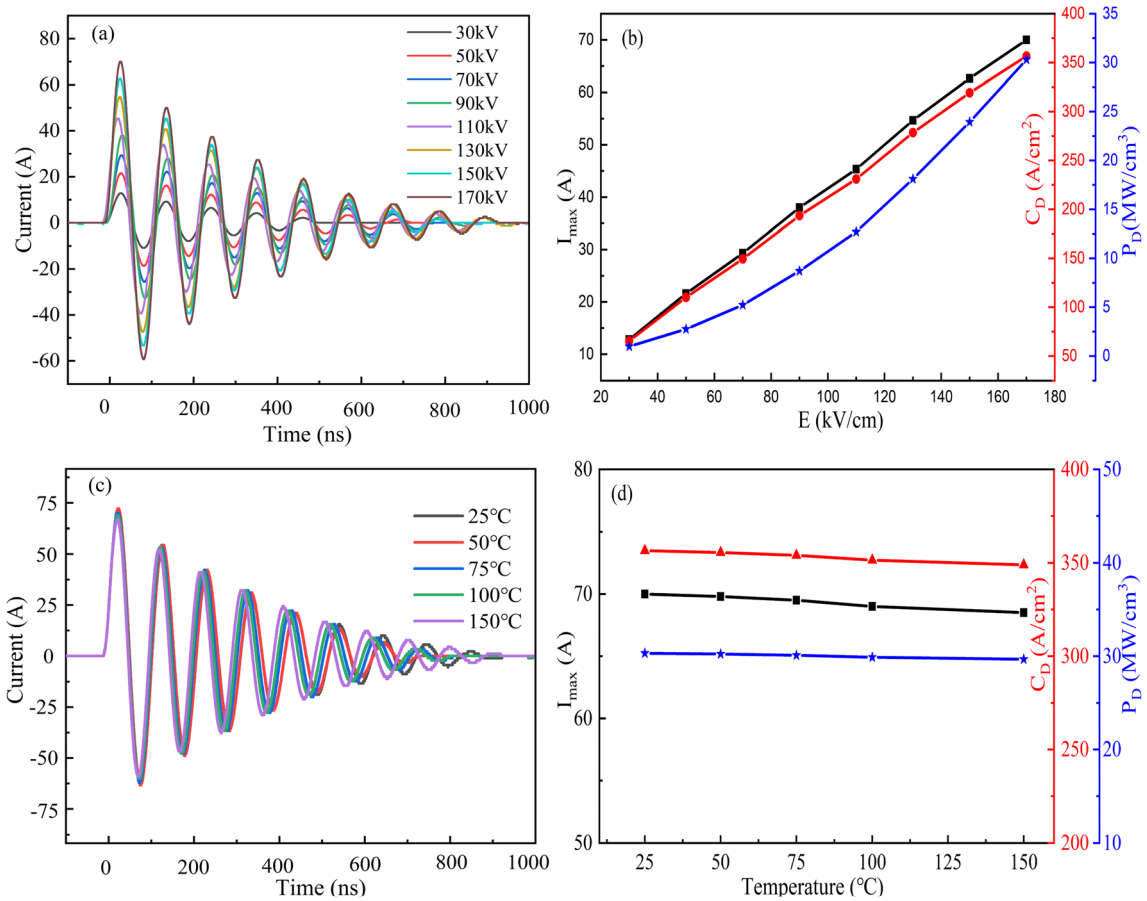

Fig. 8 **a** and **c** Discharge current waveform of 0.775BST-0.225BZN ceramic at the different electric field and different temperatures under 170 kV/cm, respectively; **b** and **d** the I_{max}, C_D and P_D as a function of the electric field E and different temperatures under 170 kV/cm

dielectric properties. The fluctuation of the I_{max}, C_D, P_D is less than 3% indicating good temperature stability of the charge–discharge character of the 0.775BST-0.225BZN ceramic. Minor fluctuation in charge–discharge property is beneficial to the 0.775BST-0.225BZN ceramic working in a wide of temperatures.

Figure 9a shows the electric field dependence of overdamped pulsed discharge electric current–time curves at room temperature. The discharge energy density (W_d) of 0.775BST-0.225BZN ceramic was calculated by [7]: $W_d = R\int i(t)^2 dt/V$, where V and R are the sample volume and total load resistor (205.5Ω), respectively. As shown in Fig. 9b, the I_{max} and W_d increase from 2.3 to 13.5 A and 0.017 to 0.554 J/cm^3

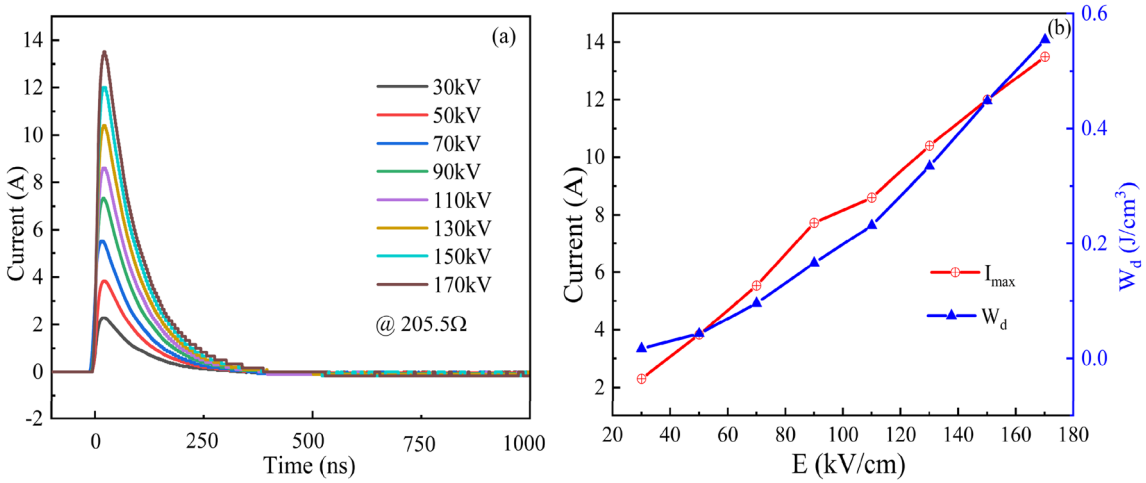

Fig. 9 **a** Discharge current waveforms of 0.775BST-0.225BZN ceramic under different electric fields at a fixed load of 205.5 Ω; **b** the I_{max} values and W_d as a function of the electric field

with the electric field increasing from 30 to 170 kV/cm, respectively. It should be noted that the energy density obtained by calculating the integrated area in *P-E* loops is slightly higher than the calculated by the charge–discharge method. The discrepancy may be attributed to the different impedance and test frequency.

4 Conclusions

A series of $(1-x)$BST-xBZN lead-free bulk ceramics were developed via a conventional solid-state synthesis route. The 0.775BST-0.225BZN ceramic was obtained at the sintering temperature as low as 1140 °C. Considering the temperature stabilization of the dielectric performances, the 0.775BST-0.225BZN ceramic meets the X8R specification and its energy storage also shows good temperature stability. Moreover, the 0.775BST-0.225BZN bulk ceramic exhibits a stable dependence of W_{st} and η on the temperature in a range of 25 °C to 150 °C. The charge–discharge properties also display good temperature stability(variations of the current density and power density are less than 3% over 25–150 °C). The lower sintering temperature and good temperature stability demonstrate that the environment-friendly 0.775BST-0.225BZN bulk ceramic is a potential candidate material for the application of the dielectric capacitor.

Acknowledgements

The author would like to thank the State Key Laboratory of Electronic Thin Films and Integrated Devices, University of Electronic Science and Technology of China (Chengdu, Sichuan, 610054, People's of China) for their help in dielectric properties testing.

References

1. W. Chen, X. Yao, X. Wei, Relaxor behavior of (Sr, Ba, Bi)TiO_3 ferroelectric ceramic. Solid State Commun. **141**, 84–88 (2007)
2. H. Cheng, H. Du, W. Zhou, D. Zhu, F. Luo, B. Xue, Bi($Zn_{2/3}Nb_{1/3}$)O_3-($K_{0.5}Na_{0.5}$)NbO_3 high temperature lead-free ferroelectric ceramics with low capacitance variation in a broad temperature usage range. J. Am. Ceram. Soc. **96**, 833–837 (2013)
3. N. Raengthon, T. Sebastian, D. Cumming, I. Reaney, D. Cann, $BaTiO_3$-Bi($Zn_{1/2}Ti_{1/2}$)O_3-$BiScO_3$ ceramics for high-temperature capacitor applications. J. Am. Ceram. Soc. **95**, 3554–3561 (2012)
4. L. Yang, X. Kong, F. Li et al., Perovskite lead-free dielectrics for energy storage applications. Prog. Mater. Sci. **102**, 72–108 (2019)
5. A. Kusko, J. Dedad, Stored energy - short-term and long-term energy storage methods. IEEE Ind. Appl. Mag. **13**, 66–72 (2007)
6. D. Wang, J. Liu, M. Zeng, C. Zhang et al., Stabilizing temperature-capacitance dependence of (Sr, Pb, Bi)TiO_3-$Bi_4Ti_3O_{12}$ solutions for energy storage. J. Am. Ceram. Soc. **102**, 4029–4037 (2019)

7. J. Li, J. Liu, M. Zeng et al., High efficiency and power density relaxor ferroelectric $Sr_{0.875}Pb_{0.125}TiO_3$ - $Bi(Mg_{0.5}Zr_{0.5})O_3$ ceramics for pulsed power capacitors. J. Eur. Ceram. Soc. **40**, 2907–2916 (2020)
8. Q. Zhang, L. Wang, J. Luo, Q. Tang, J. Du, $Ba_{0.4}Sr_{0.6}TiO_3$/MgO composites with enhanced energy storage density and low dielectric loss for solid-state pulse-forming line. Int. J. Appl. Ceram. Technol. **7**, 124–128 (2009)
9. M. Grace, R. Sambasivam, R. Perumal, V. Athikesavan, Enhanced synthesis, structure, and ferroelectric properties of Nb-modified $1–x[Bi_{0.5}(Na_{0.4}K_{0.1})(Ti_{1-x}Nb_x)]O_3–x(Ba_{0.7}Sr_{0.3})TiO_3$ ceramics for energy storage applications. J. Aust. Ceram. Soc. **56**, 157–165 (2020)
10. Y. Huang, Y. Wu, W. Qiu, J. Li, X. Chen, Enhanced energy storage density of $Ba_{0.4}Sr_{0.6}TiO_3$–MgO composite prepared by spark plasma sintering. J. Eur. Ceram. Soc. **35**, 1469–1476 (2015)
11. Y. Wang, Y. Pu, Y. Cui, Y. Shi, H. Zheng, Enhanced energy storage density of $Ba_{0.4}Sr_{0.6}TiO_3$ ceramics with additive of Bi_2O_3-B_2O_3-ZnO glass. Mater. Lett. **201**, 203–206 (2017)
12. J. Zhang, J. Zhai, H. Jiang, X. Yao, Raman and dielectric study of $Ba_{0.4}Sr_{0.6}TiO_3$-$MgAl_2O_4$ tunable microwave composite. J. Appl. Phys. **104**, 567–572 (2008)
13. Z. Song, H. Liu, Z. Wang et al., Effect of grain size on energy storage properties of $(Ba_{0.4}Sr_{0.6})TiO_3$ paraelectric ceramics. J. Eur. Ceram. Soc. **34**, 1209–1217 (2014)
14. B. Parija, T. Badapanda, S.K. Rout et al., Morphotropic phase boundary and electrical properties of $1–x[Bi_{0.5}Na_{0.5}]TiO_3–xBa[Zr_{0.25}Ti_{0.75}]O_3$ lead-free piezoelectric ceramics. Ceram. Int. **39**, 4877–4886 (2013)
15. Y. Wang, Z. Shen, Y. Li et al., Optimization of energy storage density and efficiency in $BaxSr_{1-x}TiO_3$ ($x\leq0.4$) paraelectric ceramics. Ceram. Int. **41**, 8252–8256 (2015)
16. Z. Zheng, Y. Zhang, X. Wang, Q. Zhang, I. Baturin, Variation of DC breakdown strength with phase transition temperature in $(Ba_{1-x}Sr_x)TiO_3$ ceramics. Ferroelectrics **442**, 115–122 (2013)
17. Z. Song, H. Liu, M.T. Lanagan et al., Thermal annealing effects on the energy storage properties of BST ceramics. J. Am. Ceram. Soc. **100**, 3550–3557 (2017)
18. M. Zeng, J. Liu, H. Yu et al., $NiNb_2O_6$-$BaTiO_3$ ceramics for energy-storage capacitors. Energy Technol. **6**, 899–905 (2018)
19. C. Diao, H. Liu, H. Hao, M. Cao, Z. Yao, Effect of SiO_2 additive on dielectric response and energy storage performance of $Ba_{0.4}Sr_{0.6}TiO_3$ ceramics. Ceram. Int. **42**, 12639–12643 (2016)
20. W. Li, D. Zhou, L. Pang, Enhanced energy storage density by inducing defect dipoles in lead free relaxor ferroelectric $BaTiO_3$-based ceramics. Appl. Phys. Lett. **110**, 1329021–1329025 (2017)
21. L. Wu, X. Wang, L. Li, Lead-free $BaTiO_3$–$Bi(Zn_{2/3}Nb_{1/3})O_3$ weakly coupled relaxor ferroelectric materials for energy storage. RSC Adv. **6**, 14273–14282 (2016)
22. L. Zhang, L.X. Pang, W.B. Li, D. Zhou, Extreme high energy storage efficiency in perovskite structured $(1–x)(Ba_{0.8}Sr_{0.2})$-TiO_3 - $xBi(Zn_{2/3}Nb_{1/3})O3$ ($0.04\leq x\leq0.16$) ceramics. J. Eur. Ceram. Soc. **40**, 3343–3347 (2020)
23. F. Li, J. Zhai, B. Shen et al., Influence of structural evolution on energy storage properties in $Bi_{0.5}Na_{0.5}TiO_3$-$SrTiO_3$-$NaNbO_3$ lead-free ferroelectric ceramics. J. Appl. Phys. **121**, 054103 (2017)
24. P.S. Dobal, A. Dixit, R.S. Katiyar et al., Micro-Raman study of $Ba_{1-x}Sr_xTiO_3$ ceramics. J. Raman Spectrosc. **32**, 147–149 (2001)
25. Z. Shen, X. Wang, B. Luo, L. Li, $BaTiO_3$-$BiYbO_3$ perovskite materials for energy storage applications. J. Mater. Chem. A **3**, 18146–18153 (2015)
26. D. Zheng, R. Zuo, D. Zhang et al., Novel $BiFeO_3$-$BaTiO_3$-$Ba(Mg_{1/3}Nb_{2/3})O_3$ lead-free relaxor ferroelectric ceramics for energy-storage capacitors. J. Am. Ceram. Soc. **98**, 2692–2695 (2015)
27. K. Wang, A. Hussain, W. Jo, J. Rödel, Temperature-dependent properties of $(Bi_{1/2}Na_{1/2})TiO_3$-$(Bi_{1/2}K_{1/2})TiO_3$-$SrTiO_3$ lead-free piezoceramics. J. Am. Ceram. Soc. **95**, 2241–2247 (2012)
28. H.B. Yang, F. Yan, Y. Lin, T. Wang, Improvement of dielectric and energy storage properties in $SrTiO_3$-based lead-free ceramics. J. Alloys Compd. **728**, 780–787 (2017)
29. K.N. Singh, P.K. Bajpai, Dielectric relaxation in pure columbite phase of $SrNb_2O_6$ ceramic material: impedance analysis. WJCMP **1**, 37–48 (2011)
30. T. Shi, L. Xie, L. Gu, J. Zhu, Why Sn doping significantly enhances the dielectric properties of $Ba(Ti_{1-x}Sn_x)O_3$. Sci. Rep. **5**, 8606 (2015)
31. X. Jiang, H. Hao, S. Zhang et al., Enhanced energy storage and fast discharge properties of $BaTiO_3$ based ceramics modified by $Bi(Mg_{1/2}Zr_{1/2})O_3$. J. Eur. Ceram. Soc. **39**, 1103–1109 (2019)
32. F. Li, M. Zhou, J. Zhai, B. Shen, H. Zeng, Novel barium titanate based ferroelectric relaxor ceramics with superior charge-discharge performance. J. Eur. Ceram. Soc. **38**, 4646–4652 (2018)
33. M. Zhou, R. Liang, Z. Zhou, X. Dong, Novel $BaTiO_3$-based lead-free ceramic capacitors featuring high energy storage density, high power density, and excellent stability. J. Mater. Chem. C **6**, 8528–8537 (2018)

34. X.Y. Ye, Y.M. Li, J.J. Bian, Dielectric and energy storage properties of Mn-doped $Ba_{0.3}Sr_{0.475}La_{0.12}Ce_{0.03}TiO_3$ dielectric ceramics. J. Eur. Ceram. Soc. **37**, 107–114 (2017)
35. F. Li, K. Yang, X. Liu et al., Temperature induced high charge-discharge performances in lead-free $Bi_{0.5}Na_{0.5}TiO_3$-based ergodic relaxor ferroelectric ceramics. Scr. Mater. **141**, 15–19 (2017)
36. G. Viola, R. McKinnon, V. Koval, A. Adomkevicius, S. Dunn, H. Yan, Lithium-induced phase transitions in lead-free $Bi_{0.5}Na_{0.5}TiO_3$ based ceramics. J. Phys. Chem. C **118**, 8564–8570 (2014)
37. P. Ren, Q. Wang, S. Li, G. Zhao, Energy storage density and tunable dielectric properties of $BaTi_{0.85}Sn_{0.15}O_3$/MgO composite ceramics prepared by SPS. J. Eur. Ceram. Soc. **37**, 1501–1507 (2017)